INSTITUT DE FRANCE
Académie des sciences

Comptes Rendus

Physique

Stéphane Berbenni and Ricardo A. Lebensohn

A numerical study of reversible plasticity using continuum dislocation mechanics

Volume 22, issue S3 (2021), p. 295-312

<https://doi.org/10.5802/crphys.54>

Part of the Special Issue: Plasticity and Solid State Physics

Guest editors: Samuel Forest (Mines ParisTech, Université PSL, CNRS, France) and David Rodney (Université Claude Bernard Lyon 1, France)

Les Comptes Rendus. Physique *sont membres du Centre Mersenne pour l'édition scientifique ouverte*
www.centre-mersenne.org

Comptes Rendus
Physique
2021, 22, nº S3, p. 295-312
https://doi.org/10.5802/crphys.54

Plasticity and Solid State Physics / *Plasticité et Physique des Solides*

A numerical study of reversible plasticity using continuum dislocation mechanics

Stéphane Berbenni[*, a, b] **and Ricardo A. Lebensohn**[c]

[a] Université de Lorraine, Arts et Métiers Paris Tech, CNRS, LEM3, F-57000 Metz, France

[b] Laboratory of Excellence on Design of Alloy Metals for low-mAss Structures (DAMAS), Université de Lorraine, France

[c] Theoretical Division, Los Alamos National Laboratory, Los Alamos, NM 87845, USA

E-mails: stephane.berbenni@univ-lorraine.fr (S. Berbenni), lebenso@lanl.gov (R. A. Lebensohn)

Abstract. In this contribution, an elasto-viscoplastic fast Fourier transform-based (EVPFFT) numerical implementation of the Mesoscale Field Dislocation Mechanics (MFDM) formulation, called MFDM-EVPFFT, is applied to study the reversible plastic behavior of periodic two-phase crystalline composites with an elasto-viscoplastic plastic matrix and a purely elastic second phase. Periodic laminate microstructures of this kind with different periods (i.e. sizes) are considered to examine the size dependence of the Bauschinger effect and hardening during cyclic loading. Comparisons with classic composite effects obtained with conventional crystal plasticity are discussed. Specifically, the MFDM-EVPFFT results shed light on the hardening mechanisms due to piling-up/unpiling-up of geometrically-necessary dislocations (GND) during reverse loading.

Keywords. Hardening mechanisms, Geometrically-necessary dislocations, Bauschinger effect, Size effect, FFT.

Available online 3rd March 2021

1. Introduction

Among the different physically-based micromechanical formulations/numerical methods developed in recent years to study plasticity of crystalline materials: discrete methods like discrete dislocation dynamics (DDD) [1–6], continuum approaches like strain-gradient plasticity [7–16], continuum dislocation dynamics [17–21], another continuum approach, called phenomenological Mesoscopic Field Dislocation Mechanics (MFDM) [22–28] has emerged as an efficient numerical method to model plasticity mechanisms at the mesoscopic scale, including reversible loading. MFDM combines continuum dislocation mechanics and strain-gradient crystal plasticity, integrating the mobilities of both geometrically-necessary dislocations (GNDs) and statistically-stored dislocations (SSDs). Regarding the calculation of backstress, the MFDM theory involves

* Corresponding author.

one spatial derivative of the plastic distortion, see e.g. [26], whereas other phenomenological strain-gradient plasticity theories as the ones recalled above involve two spatial derivatives, see e.g. [7, 8, 10, 12, 29]. Fundamental kinematics and thermodynamics aspects of the MFDM theory can be found elsewhere [22, 25, 30, 31]. In this mesoscale theory, the constitutive equations for slip, GND mobility, and strain-hardening need to be specified phenomenologically. MFDM requires solving the GND density transport equation, together with the stress-balance field equation, which allows the prediction of the collective arrangement and evolution of GNDs and associated long-range stresses. Originally, the MFDM theory was numerically implemented in the framework of the finite element method (FEM) [23, 26, 32–37].

More recently, an alternative numerical implementation of the MFDM theory using an approach based on fast Fourier transforms (FFT) was introduced to improve computational efficiency. FFT-based methods were originally developed and applied to composite materials [38–40], in which the mechanical heterogeneity is given by the spatial distribution of phases with different mechanical properties. Later, the method was adapted to polycrystals to accelerate crystal plasticity (CP) calculations for different constitutive behaviors and applications [41–49]. In polycrystals, the mechanical heterogeneity is related to the spatial distribution of anisotropic crystals with different orientations. These original CP FFT-based implementations showed the feasibility of efficiently solving the micromechanical behavior of complex polycrystalline unit cells. FFT-based methods were also recently extended to consider constitutive behavior based on field dislocation mechanics (FDM) [50–53] and MFDM [54–56], and were also coupled with DDD methods [57–59], providing better efficiency to these powerful and numerically-demanding formulations.

In this contribution, an elasto-viscoplastic fast Fourier transform-based method (EVPFFT) coupled with MFDM [54–56] is used to study the reversible plasticity of two-phase composites with a elasto-viscoplastic matrix and a purely elastic second phase. We consider the case of periodic laminate microstructure with various periods (i.e. sizes) and phase volume fractions of the elastic channel to examine both the effects of second phase volume fraction and channel size on the local and overall behaviors. Comparisons with corresponding results using the standard EVPFFT model with no strain-gradient effects (called in what follows CP-EVPFFT) are presented and discussed.

The plan of the paper is as follows: in Section 2 we provide details of the numerical implementation of the MFDM-EVPFFT formulation. In Section 3 we present new results of the microscopic and macroscopic responses of laminate microstructures during reverse plasticity, including the study of the Bauschinger effect and non linear hardening mechanisms due to piling-up and unpiling-up of GNDs during the forward and the reverse strain-paths. In Section 4, we provide the conclusions of this study.

2. Theory and numerical implementation

2.1. *Theory*

The displacement field $\mathbf{u}$, the strain field $\boldsymbol{\varepsilon}$, and the stress field (Cauchy stress tensor) $\boldsymbol{\sigma}$ are solved using a FFT-based micro-mechanical formulation in a small deformation setting for elasto-viscoplastic materials. It is assumed that dislocations are present and drive plastic flow within the material. Therefore, a mesoscale continuum dislocation mechanics framework is adopted to describe both dislocation kinematics and kinetics. The field equations of this problem are solved

at any material point $\mathbf{x}$ of a periodic unit cell V. The set of field equations are:

$$\begin{aligned} &\mathbf{div}\,\boldsymbol{\sigma} = 0 \\ &\boldsymbol{\sigma} = \mathbf{C} : \boldsymbol{\varepsilon}^e \\ &\mathbf{U} = \mathbf{grad}\,\mathbf{u} = \mathbf{U}^e + \mathbf{U}^p \\ &\mathbf{u} - \langle\boldsymbol{\varepsilon}\rangle \cdot \mathbf{x}\ \text{periodic}, \quad \boldsymbol{\sigma}\cdot\mathbf{n}\ \text{anti-periodic} \end{aligned} \tag{1}$$

where $\langle\cdot\rangle$ denotes a volume average over V, $\boldsymbol{\varepsilon}^e = (\mathbf{U}^e)^{\mathrm{sym}}$ and $\mathbf{C}$ is the fourth order elastic stiffness tensor, which is known at each point $\mathbf{x}$ of V. Generally, the components of the macroscopic strain $\langle\boldsymbol{\varepsilon}\rangle = \mathbf{E}$ or stress $\langle\boldsymbol{\sigma}\rangle = \boldsymbol{\Sigma}$ (or a mixed of both) are prescribed.

During plastic deformation, both the plastic distortion $\mathbf{U}^p$, which results from dislocation motion, and the elastic distortion $\mathbf{U}^e$ are incompatible fields. Depending on the resolution scale, dislocations are classified as GNDs [60] or SSDs. We make use of the MFDM formulation developed by Acharya and co-workers [22, 23, 25, 26] based on extensions of the seminal works of Kröner [61] and Mura [62]. In contrast with DDD, this theory is based on the evolution of a mesoscale value of the dislocation density tensor $\boldsymbol{\alpha}$ (also called the Nye tensor [63]) considered as a state variable [61,64]. Here, a *reduced* version of MFDM is considered [24] in the framework of the FFT-based formulation, instead of the *full* MFDM theory of Acharya and Roy [22]. Therefore, the plastic distortion rate tensor denoted $\dot{\mathbf{U}}^p$ reads:

$$\dot{\mathbf{U}}^p = \boldsymbol{\alpha} \times \mathbf{v} + \mathbf{L}^p. \tag{2}$$

The SSD mobility is represented by the mesoscale plastic distortion rate, denoted $\mathbf{L}^p$, which is defined from an averaging procedure [22, 25]. Considering a crystal plasticity framework for FCC (face-centered cubic) metals, the plastic distortion rate tensor $\mathbf{L}^p$ due to slip of SSD is given by:

$$\mathbf{L}^p = \sum_{s=1}^{N} \dot{\gamma}^s \mathbf{m}^s \tag{3}$$

where $\mathbf{m}^s$ is the crystallographic orientation tensor such that $\mathbf{m}^s = \mathbf{b}^s \otimes \mathbf{n}^s$. For each slip system s, the unit vector $\mathbf{b}^s$ denotes the slip direction and $\mathbf{n}^s$ the slip plane unit normal. N is the total number of possible slip systems in the single crystal, i.e. $N = 12$ for FCC metals deforming by $\{111\}\langle 110\rangle$ slip. The slip rate $\dot{\gamma}^s$ is defined with a viscoplastic flow rule as a power law relationship:

$$\dot{\gamma}^s = \dot{\gamma}^0 \left(\frac{|\tau^s|}{\tau_c}\right)^n \operatorname{sgn}(\tau^s) \tag{4}$$

where n is the power exponent which represents the inverse of the strain rate sensitivity of the material, $\tau^s = \mathbf{m}^s : \boldsymbol{\sigma}$ is the resolved shear stress, $\dot{\gamma}^0$ is a reference slip rate and τ_c, the reference shear stress, is considered identical for all slip systems.

The space–time evolution of the dislocation density tensor $\boldsymbol{\alpha}$ is prescribed as:

$$\dot{\boldsymbol{\alpha}} = -\mathbf{curl}\,\dot{\mathbf{U}}^p. \tag{5}$$

This hyperbolic-type equation is numerically solved with a spectral approach. In terms of the constitutive specifications of the dislocation velocity $\mathbf{v}$ and the slip distortion rate $\mathbf{L}^p$, considering plastic flow incompressibility ($\mathrm{Tr}(\mathbf{L}^p) = 0$ and $\mathrm{Tr}(\boldsymbol{\alpha}\times\mathbf{v}) = 0$, where $\mathrm{Tr}(\cdot)$ means the trace of $(\cdot)$), the GND velocity $\mathbf{v}$ reads:

$$\mathbf{v} = \frac{\mathbf{g}}{|\mathbf{g}|} v \quad \text{with } v \geq 0 \tag{6}$$

where $\mathbf{g}$ is the glide force parallel to $\mathbf{v}$ and v is the magnitude of $\mathbf{v}$. The constitutive equation adopted for v is based on the Orowan law for mobile GNDs [26]:

$$v = \frac{\zeta^2\, b}{N} \left(\frac{\mu}{\tau_c}\right)^2 \sum_{s=1}^{N} |\dot{\gamma}^s| \tag{7}$$

where ζ is a material constant, b is the magnitude of the Burgers vector, τ_c is the shear strength and μ is the isotropic elastic shear modulus of the material. From [22,26,54], $\mathbf{g}$ reads:

$$\mathbf{g} = \boldsymbol{\epsilon} : (\mathbf{S}\cdot\boldsymbol{\alpha}) - \boldsymbol{\epsilon} : \boldsymbol{\alpha}\frac{\mathbf{S}\cdot\boldsymbol{\alpha}\cdot(\boldsymbol{\alpha}^{\mathbf{t}}-\boldsymbol{\alpha})}{\boldsymbol{\alpha} : (\boldsymbol{\alpha}^{\mathbf{t}}-\boldsymbol{\alpha})} \tag{8}$$

where $\boldsymbol{\epsilon}$ denotes the third-order permutation tensor, $\mathbf{S} = \boldsymbol{\sigma} - (1/3)\mathrm{Tr}(\boldsymbol{\sigma})\boldsymbol{\delta}$ denotes the deviatoric stress tensor with $\boldsymbol{\delta}$ being the second order unit tensor.

The evolution law for the shear strength τ_c follows the strain-hardening model developed by [26,54,55]:

$$\dot{\tau}_c = \theta_0\frac{\tau_s-\tau_c}{\tau_s-\tau_0}\dot{\Gamma} + k_0\frac{\zeta^2\mu^2\, b}{2(\tau_c-\tau_0)}\left(\sum_{s=1}^{N}|\boldsymbol{\alpha}\cdot\mathbf{n}^s||\dot{\gamma}^s| + \sum_{s=1}^{N}|\boldsymbol{\alpha}\cdot\mathbf{n}^s||\boldsymbol{\alpha}\times\mathbf{v}|\right) \tag{9}$$

where $\dot{\Gamma} = |\boldsymbol{\alpha}\times\mathbf{v}| + \sum_{s=1}^{N}|\dot{\gamma}^s|$, τ_0 is the yield strength due to lattice friction (which is very low for FCC metals), τ_s is the saturation stress, θ_0 is the stage II hardening rate for FCC metals, k_0 is related to a geometric mean free path due to GND forest on slip system s.

2.2. *FFT-based numerical implementation*

The FFT-based MFDM numerical implementation starts from the small-strain elasto-viscoplastic crystal plasticity formulation [44]. Using a backward Euler implicit time discretization and Hooke's law, the expression of the stress tensor $\boldsymbol{\sigma}$ at $t+\Delta t$ is given by:

$$\boldsymbol{\sigma}^{t+\Delta t} = \mathbf{C} : \boldsymbol{\varepsilon}^{e,t+\Delta t} = \mathbf{C} : (\boldsymbol{\varepsilon}^{t+\Delta t} - \boldsymbol{\varepsilon}^{p,t} - \dot{\boldsymbol{\varepsilon}}^{p,t+\Delta t}(\boldsymbol{\sigma}^{t+\Delta t})\Delta t). \tag{10}$$

In what follows, the supra-indices $t+\Delta t$ are omitted, and only the fields corresponding to the previous time step t will be explicitly indicated. The unknown total strain field $\boldsymbol{\varepsilon}$ is solved through an integral Lippmann–Schwinger–Dyson equation for the unknown strain field $\boldsymbol{\varepsilon}$:

$$\boldsymbol{\varepsilon}(\mathbf{x}) = \langle\boldsymbol{\varepsilon}\rangle - \int_V \boldsymbol{\Gamma}^0(\mathbf{x}-\mathbf{x}') : \boldsymbol{\tau}(\mathbf{x}')\,\mathrm{d}V' \tag{11}$$

where $\langle\boldsymbol{\varepsilon}\rangle$ represents the average value of $\boldsymbol{\varepsilon}$ in V, $\boldsymbol{\Gamma}^0$ is the modified Green tensor associated with a homogeneous elastic stiffness $\mathbf{C}^0$ and $\boldsymbol{\tau} = \boldsymbol{\sigma} - \mathbf{C}^0 : \boldsymbol{\varepsilon}$ is the stress polarization field. In what follows, Equation (11) is solved using a numerical scheme based on FFT and augmented Lagrangians [40]. Let $\boldsymbol{\xi}$ be the Fourier vector of magnitude $\xi = \sqrt{\boldsymbol{\xi}\cdot\boldsymbol{\xi}}$ and i the complex imaginary number $\mathrm{i} = \sqrt{-1}$. Let $\widehat{\boldsymbol{\varepsilon}}(\boldsymbol{\xi})$ and $\widehat{\boldsymbol{\Gamma}}^0(\boldsymbol{\xi})$ be, respectively, the Fourier transform of $\boldsymbol{\varepsilon}(\boldsymbol{x})$ and $\boldsymbol{\Gamma}^0(\mathbf{x})$. The Fourier transform of the integral equation (11) yields:

$$\begin{aligned} &\widehat{\boldsymbol{\varepsilon}}(\boldsymbol{\xi}) = -\widehat{\boldsymbol{\Gamma}}^0(\boldsymbol{\xi}) : \widehat{\boldsymbol{\tau}}(\boldsymbol{\xi}) \quad \forall\boldsymbol{\xi}\neq\mathbf{0} \\ &\widehat{\boldsymbol{\varepsilon}}(\mathbf{0}) = \langle\boldsymbol{\varepsilon}\rangle. \end{aligned} \tag{12}$$

The Green operator associated with $\mathbf{C}^0$ in Fourier space, $\widehat{\boldsymbol{\Gamma}}^0$, is given in [39,65].

Let us assume now that $\boldsymbol{\lambda}^{(n)}$ and $\mathbf{e}^{(n)}$ are, respectively, the auxiliary guess stress and strain fields at iteration (n). The stress polarization tensor becomes: $\boldsymbol{\tau}^{(n)} = \boldsymbol{\lambda}^{(n)} - \mathbf{C}^0 : \mathbf{e}^{(n)}$. An alternative fixed-point expression, which requires computing the Fourier transform of the stress field instead of that of the polarization field was reported in [40]:

$$\begin{aligned} &\widehat{\mathbf{e}}^{(n+1)}(\boldsymbol{\xi}) = \widehat{\mathbf{e}}^{(n)}(\boldsymbol{\xi}) - \widehat{\boldsymbol{\Gamma}^0}(\boldsymbol{\xi}) : \widehat{\boldsymbol{\lambda}}^{(n)}(\boldsymbol{\xi}) \quad \forall\boldsymbol{\xi}\neq\mathbf{0} \\ &\widehat{\mathbf{e}}^{(n+1)}(\mathbf{0}) = \langle\boldsymbol{\varepsilon}^{(n)}\rangle. \end{aligned} \tag{13}$$

Once $\mathbf{e}^{(n+1)} = \mathrm{FFT}^{-1}(\widehat{\mathbf{e}}^{(n+1)}(\boldsymbol{\xi}))$ is obtained in real space by using the inverse Fourier transform (FFT^{-1}), the nullification of the residual $\mathbf{R}$, which depends on the stress and strain tensors $\boldsymbol{\sigma}^{(n+1)}$ and $\boldsymbol{\varepsilon}^{(n+1)}$, is solved:

$$\mathbf{R}(\boldsymbol{\sigma}^{(n+1)}) = \boldsymbol{\sigma}^{(n+1)} + \mathbf{C}^0 : \boldsymbol{\varepsilon}^{(n+1)}(\boldsymbol{\sigma}^{(n+1)}) - \boldsymbol{\lambda}^{(n)} - \mathbf{C}^0 : \mathbf{e}^{(n+1)} = 0. \tag{14}$$

This nonlinear equation was solved in [44] using a Newton–Raphson scheme. The $(p+1)$-guess for the stress field $\boldsymbol{\sigma}^{(n+1)}$ is given by:

$$\boldsymbol{\sigma}^{(n+1,p+1)} = \boldsymbol{\sigma}^{(n+1,p)} - \left(\left(\frac{\partial \mathbf{R}}{\partial \boldsymbol{\sigma}}\right)_{\boldsymbol{\sigma}^{(n+1,p)}}\right)^{-1} : \mathbf{R}(\boldsymbol{\sigma}^{(n+1,p)}). \tag{15}$$

Using the constitutive equation, the Jacobian matrix in the above expression reads:

$$\left(\frac{\partial \mathbf{R}}{\partial \boldsymbol{\sigma}}\right)_{\boldsymbol{\sigma}^{(n+1,p)}} = \boldsymbol{\delta} \otimes \boldsymbol{\delta} + \mathbf{C}^0 : \mathbf{C}^{-1} + \Delta t\, \mathbf{C}^0 : \left(\frac{\partial \dot{\boldsymbol{\varepsilon}}^p}{\partial \boldsymbol{\sigma}}\right)_{\boldsymbol{\sigma}^{(n+1,p)}} \tag{16}$$

where $\otimes$ is the dyadic (or tensorial) product.

The expression of $\partial \dot{\boldsymbol{\varepsilon}}^p / \partial \boldsymbol{\sigma}$ was already reported in [54, 55] for the numerical MFDM-EVPFFT formulation. Once the convergence is achieved on $\boldsymbol{\sigma}^{(n+1)}$ and $\boldsymbol{\varepsilon}^{(n+1)}$, the new guess for the auxiliary stress field $\boldsymbol{\lambda}$ is given by using the Uzawa descent algorithm:

$$\boldsymbol{\lambda}^{(n+1)} = \boldsymbol{\lambda}^{(n)} + \mathbf{C}^0 : (\mathbf{e}^{(n+1)} - \boldsymbol{\varepsilon}^{(n+1)}). \tag{17}$$

The iterative procedure stops when the normalized average differences between the stress fields $\boldsymbol{\sigma}$ and $\boldsymbol{\lambda}$, and the strain fields $\boldsymbol{\varepsilon}$ and $\mathbf{e}$, are smaller than a given threshold error (typically 10^{-5}). This condition implies the fulfillment of both stress equilibrium and strain compatibility up to sufficient accuracy. The FFT-based resolution of the Lippmann–Schwinger–Dyson equation used a DFT-scheme coupled to a rotated centered finite difference scheme [65]. In the algorithm described above, an overall macroscopic strain $\mathbf{E} = \langle \boldsymbol{\varepsilon}^{(n)} \rangle$ is applied to the periodic unit cell V in the form of:

$$\mathbf{E} = \mathbf{E}^t + \dot{\mathbf{E}} \Delta t. \tag{18}$$

In cases of mixed boundary conditions with imposed macroscopic strain rate $\dot{\mathbf{E}}$ and stress $\boldsymbol{\Sigma}$, the $(n+1)$-guess of the macroscopic strain $\mathbf{E}^{(n+1)}$ was given in [40, 44].

Let $\widehat{\boldsymbol{\alpha}}(\boldsymbol{\xi})$ be the Fourier transform of $\boldsymbol{\alpha}(\boldsymbol{x})$. Following [52, 54], it reads at $t + \Delta t$ in component form:

$$\widehat{\alpha}_{ij}^{t+\Delta t} = \kappa(\eta)(\widehat{\alpha}_{ij}^{t} - \Delta t\, \mathrm{i}\, \xi_k\, (\widehat{(\alpha_{ij} v_k)}^{t} - \widehat{(\alpha_{ik} v_j)}^{t})) - \Delta t\, \mathrm{i}\, \xi_k\, e_{jkl} \widehat{(L_{il}^p)}^{t} \tag{19}$$

where an exponential second order spectral low-pass filter was used to stabilize the numerical approximation of by eliminating high frequencies leading to spurious oscillations. The exponential filter is defined as function of discrete frequencies η as:

$$\kappa(\eta) = \exp(-\beta(\eta)^{2p}) \tag{20}$$

where the damping parameter β is defined as $\beta = -\log \varepsilon_M$, where ε_M is low value parameter that was optimized in [52]. To fix the time step Δt in (19) to satisfy stability requirements for numerically solving the dislocation density transport equation, a user-specified fraction denoted $c = 0.25$ of Courant–Friedrichs–Lewy (CFL) limit is used in the numerical applications such that:

$$\Delta t_{\mathrm{CFL}} = c \frac{\delta}{v_{\max}} \tag{21}$$

where δ is the voxel size and $v_{\max}$ is the maximal GND velocity. The time step is given as $\Delta t = \min(\Delta t_{\mathrm{CFL}}, \Delta t_\varepsilon)$ where Δt_{CFL} and the time step Δt_ε is the time step classically used in the EVPFFT formulation.

3. Results and discussion

3.1. *Two-phase periodic laminate microstructures*

We discuss here reversible plasticity predictions using the MFDM-EVPFFT formulation. As illustrative example, a two-phase periodic laminate composite with period H along the y-direction

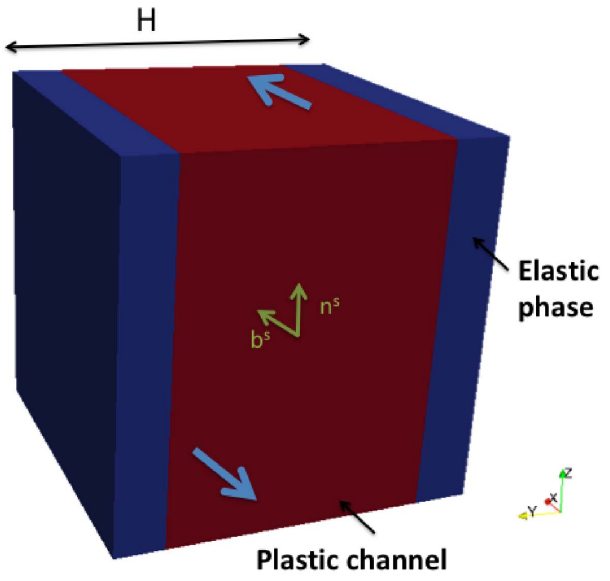

Figure 1. Two-phase periodic laminate composite with period H along the y-direction. The red region is the plastic channel and the blue regions represent elastic second phase. The blue arrows describe the shear loading, and, the green arrows show the unit slip direction and normal vectors of the active slip system.

Table 1. List of plastic material parameters used for numerical simulations for the channel phase

$\dot{\gamma}^0$ (s^{-1})	n	ζ	b (m)	τ_0 (MPa)	τ_s (MPa)	θ_0 (MPa)	k_0
1	20	0.33	2.86×10^{-10}	3	12	150	20 or 500

as the one shown in Figure 1 is subjected to forward and reverse shear loading. The unit vectors along the x-, y-, z-directions are denoted $\mathbf{e}_1$, $\mathbf{e}_2$ and $\mathbf{e}_3$, respectively. The two-phase composite consists of a purely elastic phase (hereafter called *second phase* and denoted P) and an elasto-viscoplastic phase (hereafter called *plastic channel* denoted C). The volume fraction of the second phase P is denoted f. Similar microstructures were already studied in [54] but only for monotonic loadings. Here, three different periods H are considered: $H = 0.25$ μm, $H = 1$ μm, $H = 10$ μm. The unit cell is discretized into $32^3 = 32\,768$ voxels, which is sufficient for such simple microstructure [54].

Elasticity is assumed to be isotropic and homogeneous with Young's modulus $E = 69$ GPa and Poisson ratio $\nu = 0.33$ as for aluminium. Therefore, the elastic shear modulus is $\mu = 25.94$ GPa. For the plastic channel, the viscoplastic material parameters used for numerical simulations are reported in Table 1. Let us note that the effect of the phenomenological parameter k_0 in (9) will be studied considering two different values: $k_0 = 20$ or $k_0 = 500$. The numerical parameters used for GND density evolution equation are taken from [52], where these parameters were optimized. Here, we consider $c = 0.25$, $\varepsilon_M = 0.2$, $p = 1$. The unit cell undergoes pure shear loadings in the following sequence: forward shear up to +0.2%/reverse shear up to −0.2%/forward shear up to +0.2%. The applied shear strain rates are $\dot{E}_{13} = \dot{E}_{31} = \pm 0.001\ s^{-1}$ with $\Delta t_\varepsilon = 0.01$ s. The crystallographic orientation of the plastic single crystal channel is given by the three Bunge–Euler angles: $\phi_1 = 300°$, $\phi = 54.7358°$, $\phi_2 = 45°$, which leads to a predominant single slip mode in

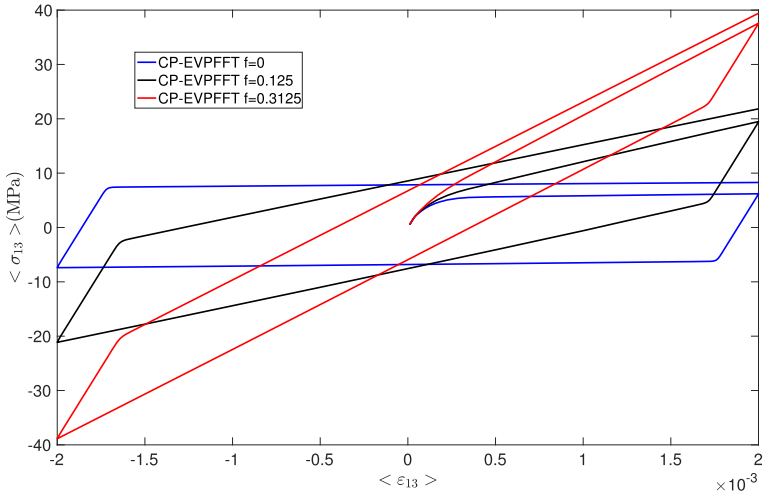

Figure 2. Effect of second elastic phase volume fraction f with CP-EVPFFT on the cyclic shear response of two-phase laminate microstructures.

the channel due to the slip system $(111)\langle 10\bar{1}\rangle$. This active slip system is represented in Figure 1 by two arrows in the plastic channel, representing the unit normal $\mathbf{n}^s$, and, the unit vector in the slip direction $\mathbf{b}^s$. Both are parallel to $\mathbf{e}_3$ and $\mathbf{e}_1$, respectively. In this configuration, using the MFDM-EVPFFT model, the main GND density created during this forward/reverse/forward shear loading is due to the screw component of the Nye tensor α_{11} with GND density defined by α_{11}/b (in m^{-2}). In contrast with conventional crystal plasticity, the evolution equations in the MFDM theory impose a jump condition on the plastic distorsion rate across the material interfaces [66]. This jump condition is specified to describe the interaction of dislocations with impenetrable elastic/plastic interfaces, which corresponds to fully constrained plastic flow at the interface [26]. Therefore, the condition on the interface is $\dot{\mathbf{U}}^p \times \mathbf{n} = 0$, where $\mathbf{n} = \mathbf{e}_2$ is the unit normal to the interface. Using Cartesian coordinates, the interfacial condition for voxels in the plastic channel adjacent to the interface is: $\dot{U}^p_{ij} = 0$ except $\dot{U}^p_{12} \neq 0$ and $\dot{U}^p_{32} \neq 0$.

3.2. *Cyclic plasticity responses obtained with CP-EVPFFT*

Let us first examine the classic composite effect (i.e. associated with the volume fraction f) on the reversible behavior of the two-phase laminate composite, obtained with conventional crystal plasticity. It corresponds to $\boldsymbol{\alpha} = \mathbf{0}$ in (9) and $\mathbf{v} = \mathbf{0}$ in (6), i.e. $\dot{\mathbf{U}}^p = \mathbf{L}^p$, and there is no condition on the plastic distorsion rate across the material interfaces. The model is then reduced to the classic CP-EVPFFT formulation as described in [44] which is size (H-) independent, because there is no internal length scale. As reported in Figure 2, the overall shear responses are only dependent on the second phase volume fraction f. When f is increased from $f = 0$ to $f = 0.125$ and $f = 0.3125$, the overall hardening rate during forward and reverse shearing increases. The case $f = 0$ corresponds to the single crystal's response, which only exhibits a small isotropic hardening contribution due to chosen parameters τ_0, τ_s and θ_0 in Table 1. It is observed on Figure 2 that the Bauschinger effect increases with f. Following [67,68], the stress reflecting the Bauschinger effect is defined as $\Sigma_b = (\Sigma_f - \Sigma_r)/2$, where Σ_f is here the forward shear stress Σ_{13} at $E_{13} = 0.2\%$ (in the plastic regime) and Σ_r is the reverse shear stress Σ_{13} at the onset of plasticity during reverse loading. According to Figure 2, a rapid elastic/plastic transition is obtained with CP-EVPFFT when Σ_r is reached. Here, $\Sigma_b = 0$ MPa for $f = 0$ (single crystal), $\Sigma_b = 12.1$ MPa for

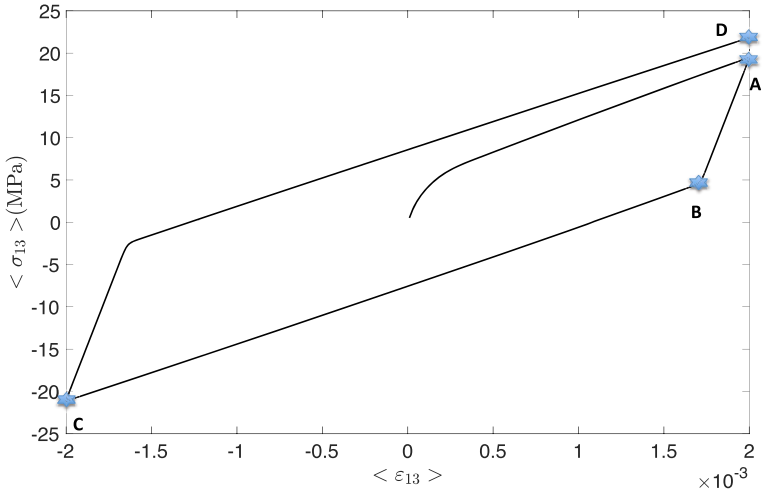

Figure 3. Cyclic shear stress response for $f = 0.125$ obtained with CP-EVPFFT describing the 4 different states: state A (at the end of the first forward shear loading at $E_{13} = 0.2\%$), state B (during the reverse shear loading at $E_{13} = 0.17\%$), state C (at the end of the reverse shear loading at $E_{13} = -0.2\%$), state D (at the end of the second forward shear loading at $E_{13} = 0.2\%$).

$f = 0.125$ (with $\Sigma_f = 19.4$ MPa and $\Sigma_r = -4.8$ MPa) and $\Sigma_b = 30.15$ MPa for $f = 0.3125$ (with $\Sigma_f = 37.6$ MPa and $\Sigma_r = -22.7$ MPa). The negative sign for Σ_r stems from the fact that the onset of plastic yielding during reverse shear loading occurs in the positive stress quadrant in Figure 2 (and not in the negative stress quadrant), which is the signature of a strong Bauschinger effect and a large linear kinematic hardening for such volume fractions of elastic phase. This is also the clear signature of a large *permanent softening*, which was for example reported in [67] for copper crystals reinforced with silica particles.

When $f = 0.125$ or $f = 0.3125$, the observed strong Bauschinger effect is due to backstress (or kinematic hardening) denoted X. In both phases, the residual stresses $R^{P,C} = \sigma_{13}^{P,C} - \Sigma_{13}$ are constant and can be calculated from the stress average rule: $\Sigma_{13} = \langle\sigma_{13}\rangle = f\sigma_{13}^P + (1-f)\sigma_{13}^C$ using the compatibility condition for an infinite planar grain boundary, as given in [69]:

$$\begin{aligned} R^P &= \sigma_{13}^P - \Sigma_{13} = 2\mu(1-f)\varepsilon_{13}^p \\ R^C &= \sigma_{13}^C - \Sigma_{13} = -2\mu f\varepsilon_{13}^p \end{aligned} \tag{22}$$

where ε_{13}^p is the uniform plastic shear strain in the channel. In this configuration, $\varepsilon_{13}^p = U_{13}^p/2$, since $U_{31}^p = 0$. For this two phase composite under pure shear loading, the kinematic hardening X is given by the difference between the macroscopic shear stress Σ_{13} and the shear stress in the plastic channel σ_{13}^C, therefore $X = 2\mu f\varepsilon_{13}^p$. Since the macroscopic plastic shear strain is $E_{13}^p = (1-f)\varepsilon_{13}^p$, the kinematic hardening is given by $X = 2\mu(f/(1-f))E_{13}^p$. Therefore, a linear kinematic hardening modulus (i.e. hardening slope) of $2\mu(f/(1-f))$ is obtained. This value was verified for both volume fractions $f = 0.125$ and $f = 0.3125$ with the classic CP-EVPFFT model using Figure 2. Such hardening slope was also reported by Mughrabi [70]. From Figure 3 in the case of $f = 0.125$, the evolution of the plastic distortion U_{13}^p and shear stress σ_{13} are studied at 4 different loading states (denoted A, B, C, D) during one shear loading cycle, i.e. forward/reverse/forward shear for one cycle. Figures 4 and 5 describe the spatial variations of U_{13}^p and σ_{13}, respectively, along the y direction for A, B, C, D. Figure 4 shows that the plastic distortion is uniform in the channel and this result is independent of the spatial period H. At macroscopic shear strain $E_{13} = \langle\varepsilon_{13}\rangle = 0.2\%$

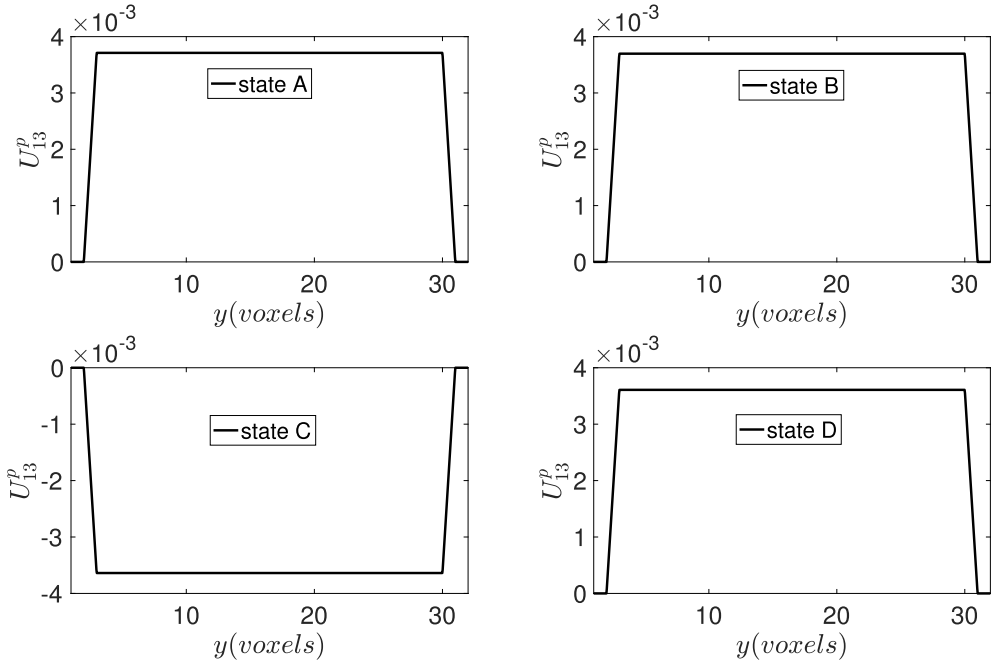

Figure 4. Spatial variations along the y-axis in voxels of the plastic distortion U^p_{13} at the 4 different states: A, B, C, D.

(i.e. at the end of forward loading), it is seen from Figure 5 that $\sigma^P_{13} = 103.7$ MPa and $\sigma^C_{13} = 7.4$ MPa. The macroscopic shear stress is $\Sigma_{13} = 19.4$ MPa, therefore the residual stresses in both phases are $R^P = 84.3$ MPa and $R^C = -12$ MPa, respectively. From Figure 4, $U^p_{13} = 0.37\%$ at $E_{13} = \langle\varepsilon_{13}\rangle = 0.2\%$ (i.e. $\varepsilon^p_{13} = 0.185\%$ at A), i.e. Equation (22) are satisfied.

Using the incompatibility relation $\boldsymbol{\alpha} = \mathbf{curl}\ \mathbf{U^e}$ [61, 64] solved in the Fourier space with a centered finite difference scheme (see numerical details in [51, 54]), the profiles of the GND density α_{11}/b are obtained at the different states. Figure 6 shows a rapid change of sign from state B for the GND densities during reverse loading compared to the ones at state A. This leads to an inversion of plastic incompatibilities at the interfaces in the transition between A and C. Such GND densities are low in magnitude with maximal values around 2×10^{10} m^{-2} and they correspond to interfacial GND densities [71]. Therefore, CP-EVPFFT predicts no development of GND pile ups and the relaxation of piecewise constant internal stresses during the transition between forward and reverse strain paths (see Figure 5) explains the rapid transition to a linear *permanent softening* after the onset of plasticity during reverse loading, i.e. after Σ_r.

3.3. *Cyclic plasticity responses obtained with MFDM-EVPFFT*

Let us consider the case where the volume fraction of elastic second phase is set to $f = 0.125$ with three different periods: $H = 0.25$ µm, $H = 1$ µm, $H = 10$ µm. The role of the material parameter k_0 in (9) is first examined. This parameter is a fitting parameter used in the phenomenological MFDM formulation to modulate the effect of GND densities on the material's isotropic hardening. An increase of k_0 means a decrease of the geometric mean-free path due to forest GND. Figures 7 and 8 report a *"smaller is stronger"* size effect observed on both Σ_f (at $E_{13} = 0.2\%$) and Σ_b for $k_0 = 20$ and $k_0 = 500$, respectively. Comparing the values reported in Tables 2 and 3, this

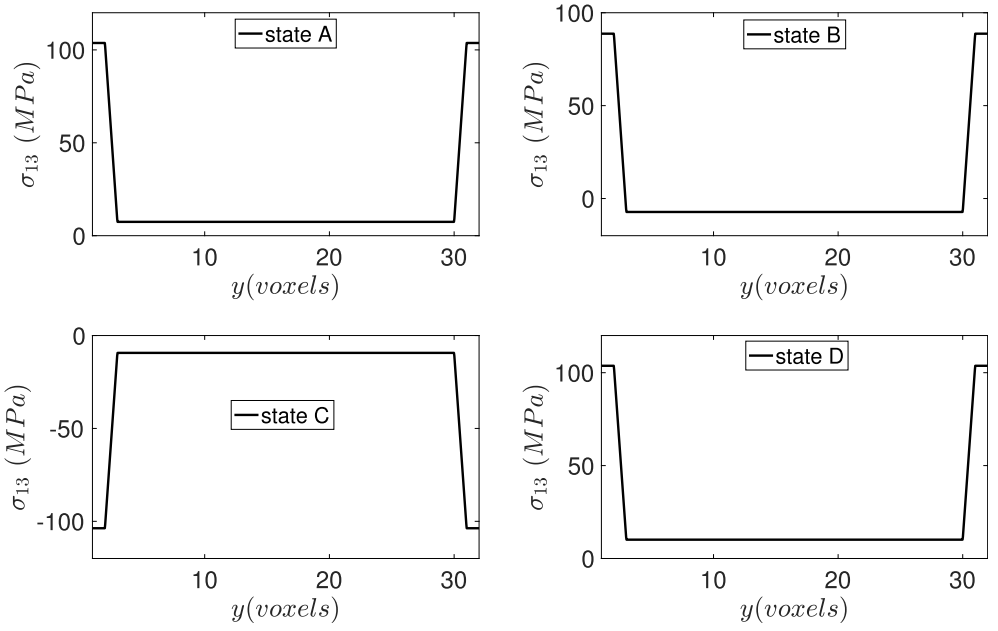

Figure 5. Spatial variations along the y-axis in voxels of the shear stress σ_{13} at the 4 different states: A, B, C, D.

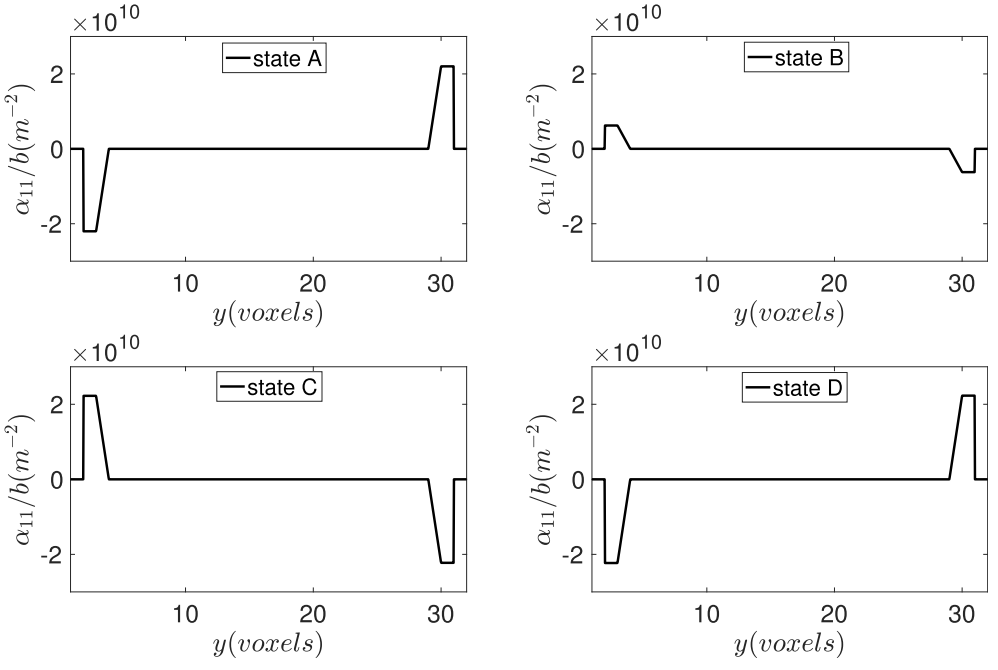

Figure 6. Spatial variations along the y-axis in voxels of the GND density α_{11}/b at the 4 different states: A, B, C and D.

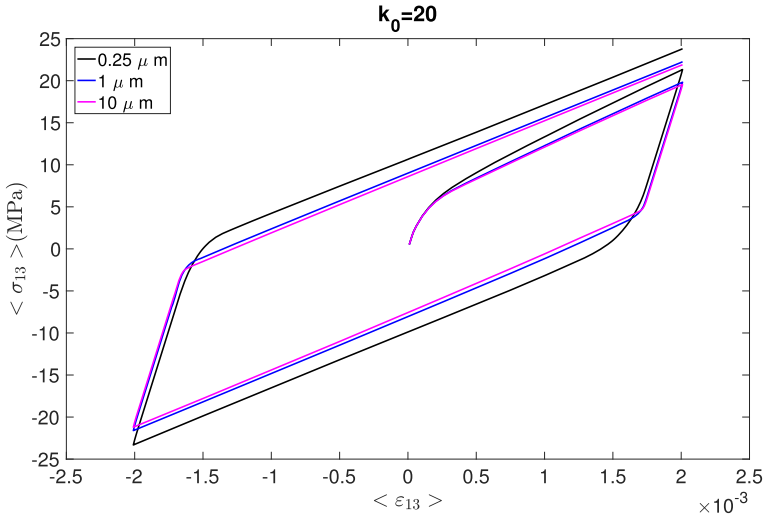

Figure 7. Effect of period H (H = 0.25 μm, H = 1 μm, H = 10 μm) with MFDM-EVPFFT for an elastic phase volume fraction f = 0.125 on the cyclic shear response of two-phase laminate microstructures. The value of k_0 is set to k_0 = 20.

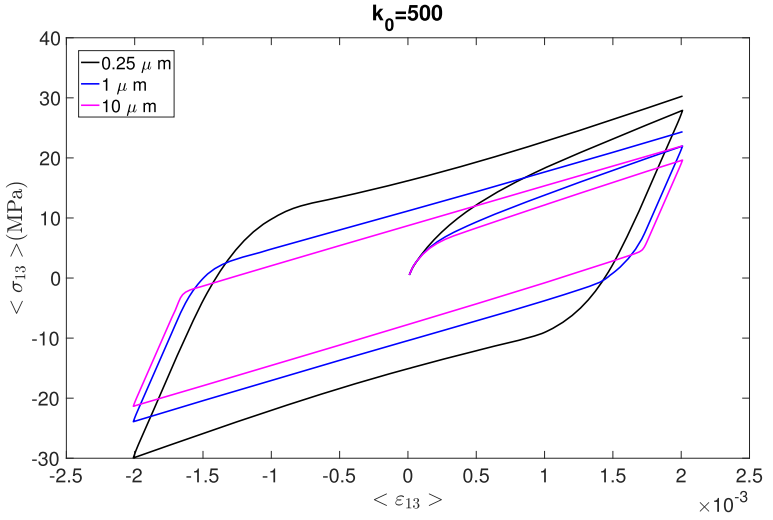

Figure 8. Effect of period H (H = 0.25 μm, H = 1 μm, H = 10 μm) with MFDM-EVPFFT for an elastic phase volume fraction f = 0.125 on the cyclic shear response of two-phase laminate microstructures. The value of k_0 is set to k_0 = 500.

size effect is more pronounced for k_0 = 500. When H is large, it is also observed that the *permanent softening* during reverse loading rapidly converges to the CP-EVPFFT result (Figure 3). Conversely, for the smallest size (H = 0.25 μm), a larger *transient softening* occurs before *permanent softening*, as reported for example in [68] for particulate reinforced Al alloys. It corresponds to a larger rounded stress/strain response, which is observed between states A and B. This transient softening is due to a more gradual onset of plasticity during reverse shear due to plastic strain gradients in plastic channels. This effect is even more pronounced in the case of k_0 = 500 in Figure 9, where the presence of inflection points is also reported during the first reverse loading and

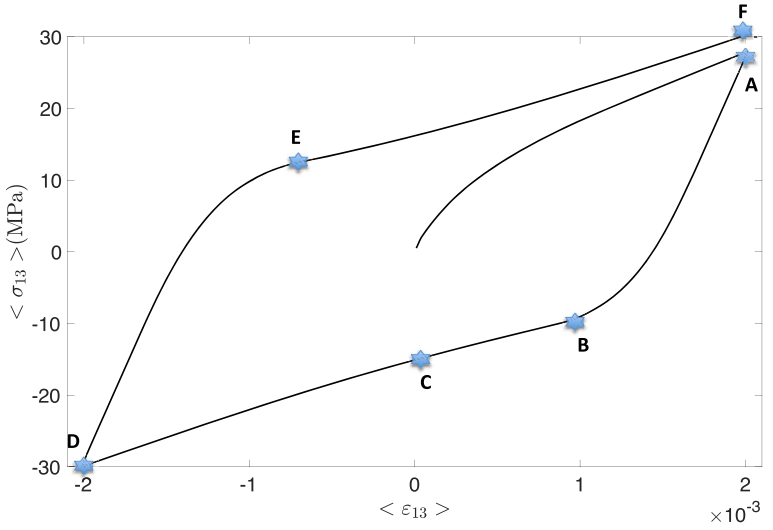

Figure 9. Cyclic shear stress response for $f = 0.125$ obtained with the MFDM-EVPFFT model describing 6 different subsequent states: state A (at the end of the first forward shear loading at $E_{13} = 0.2\%$), state B (during the reverse shear loading at $E_{13} = 0.1\%$), state C (during the reverse shear loading at $E_{13} = 0\%$), state D (at the end of the reverse shear loading second forward shear loading at $E_{13} = -0.2\%$), state E (during the second forward shear loading at $E_{13} = -0.07\%$), state F (at the end of the second forward shear loading at $E_{13} = 0.2\%$).

Table 2. Values of Σ_f (at $E_{13} = 0.2\%$) and Σ_b for $k_0 = 20$ obtained with the MFDM-EVPFFT formulation

H	0.25 µm	1 µm	10 µm
Σ_f (MPa)	21.3	19.8	19.5
Σ_b (MPa)	13.8	12.55	12.3

Table 3. Values of Σ_f (at $E_{13} = 0.2\%$) and Σ_b for $k_0 = 500$ obtained with the MFDM-EVPFFT formulation

H	0.25 µm	1 µm	10 µm
Σ_f (MPa)	27.9	22	19.6
Σ_b (MPa)	16.6	14.25	12.35

during last forward loading to form a hysteresis loop. However, it is noteworthy that the loop is not completely closed since the hardening is not purely kinematic due to the presence of the isotropic intra-crystalline hardening contribution in the model, see (9).

In contrast with strain gradient plasticity and Cosserat models, such as the ones described by Forest [72], the present formulation does not provide an *explicit* expression of intra-crystalline backstress involving the *second derivative of slip* in the channel. This explicit dependence stems from the presence of a couple stress tensor in the balance of moment of momentum. In addition, a constitutive relationship between the couple stress tensor and the curvature tensor is applied, where the curvature tensor is related to the Nye tensor [61, 63, 64]. Interestingly, a link was made in [72] with the linear kinematic hardening modulus obtained from the dislocation model

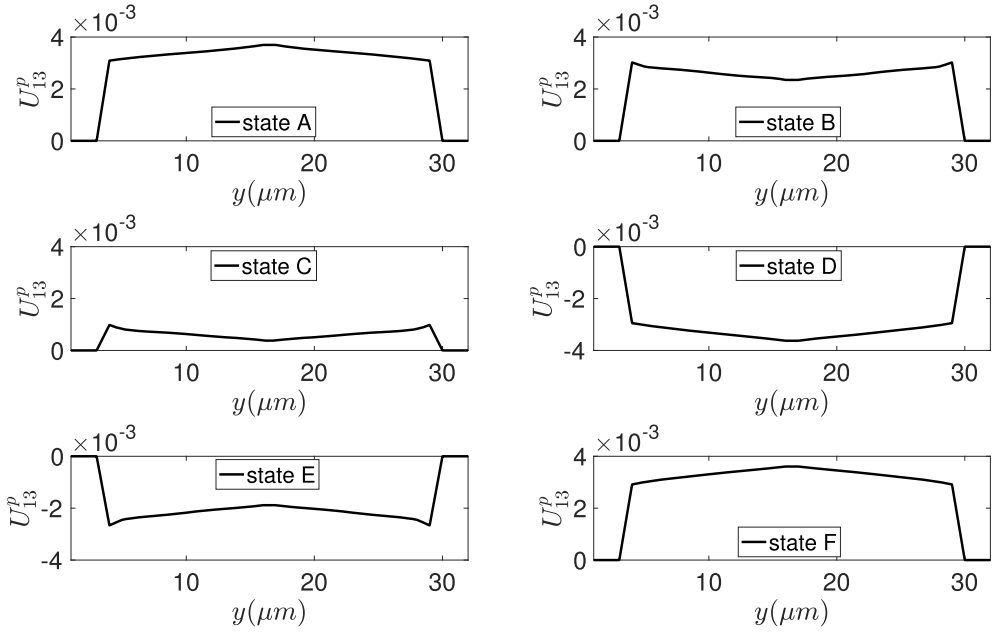

Figure 10. Spatial variations along the y-axis in voxels of the plastic distortion U^p_{13} at the 6 different states: A, B, C, D, E and F (see Figure 9) for $H = 0.25$ μm and $k_0 = 500$.

of Tanaka and Mura [73], based on the static equilibrium of a double-ended edge dislocation pile-up.

In what follows, the evolution of internal fields at 6 different states are studied for $H = 0.25$ μm and $k_0 = 500$. These states are denoted A, B, C, D, E and F in Figure 9. In order to explain the transient softening phenomenon with inflection points, obtained with the MFDM-EVPFFT model, let us consider the spatial variation along the y-direction of the plastic distortion U^p_{13}, the shear stress σ_{13} and the screw GND density component α_{11}/b. According to the MFDM-EVPFFT results, the plastic distortion and the stress profiles reported in Figures 10 and 11 respectively exhibit a spatial gradient in the y-direction of the channel in contrast with the CP-EVPFFT model (see Figure 4). Interestingly, the intra-crystalline slip gradients change sign when the strain is reversed. This can be observed in Figure 10 with a gradual interchange of profile slopes from the middle of the channel to the boundaries, between states A and B/C, or, between D and E/F. These changes in slopes and the inflexion points observed in the macroscopic response can be explained from the evolution of the GND density component α_{11}/b, discussed next.

The GND density α_{11}/b as a function of y (in voxels) at the 6 different states is shown in Figure 12. At state A, a continuous screw double-ended GND pile up is first built up at the end of the first forward shear loading, with maximal magnitudes for α_{11}/b near phase boundaries equal to 7.8×10^{13} m^{-2}. At state B, an unpiling-up mechanism operates with the progressive annihilation of the screw GND density built up at stage A. At stage C, which corresponds to a state after the inflection point observed on the reverse shear/strain curve, a GND pile up with opposite polarities progressively forms, up to stage D. At stage E, which corresponds to the start of the second forward loading in the hysteresis curve, the unpiling-up mechanism operates again with the progressive removal of the GND density built up at stage D. Finally, at stage F, a double-ended GND pile up with same polarities as the ones formed at the end of stage A is restored and is similar to one formed at the end of stage A. This can be attributed to a plastic

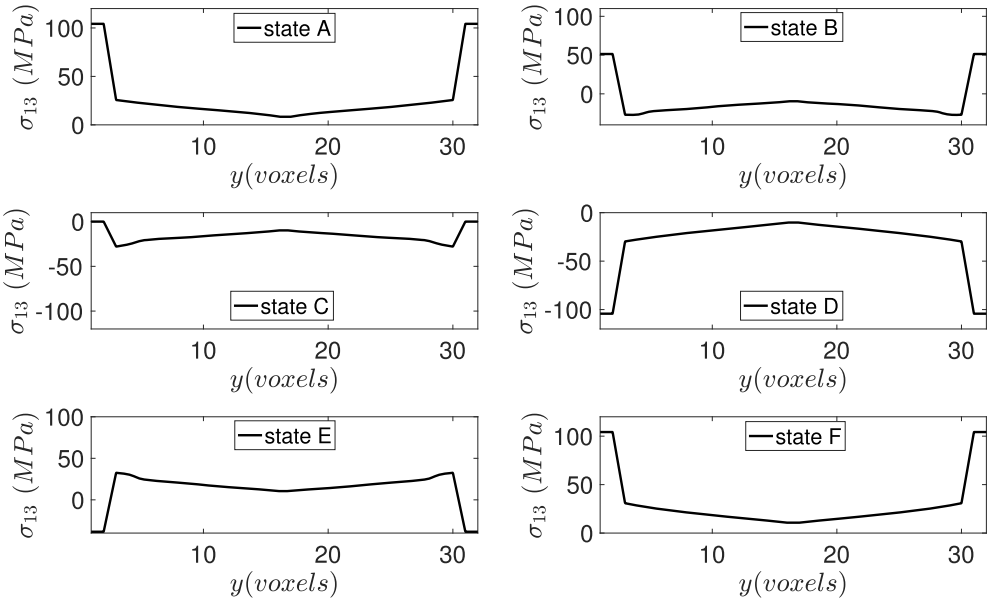

Figure 11. Spatial variations along the y-axis in voxels of the shear stress σ_{13} at the 6 different states: A, B, C, D, E and F (see Figure 9) for $H = 0.25$ μm and $k_0 = 500$.

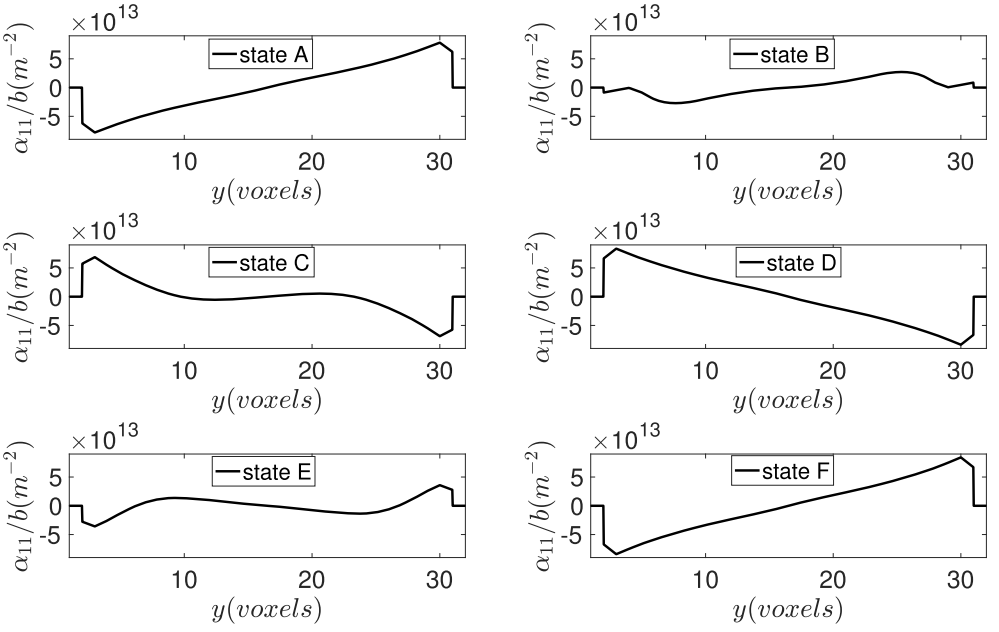

Figure 12. Spatial variations along the y-axis (in voxels) of the GND density α_{11}/b at the 6 different states: A, B, C, D, E and F (see Figure 9) for $H = 0.25$ μm and $k_0 = 500$.

memory during cyclic loading and a non linear development of internal stresses due to piling-up/unpiling-up mechanisms as reported by Asaro [74]. Experimental evidence of this specific hardening with concave shape was reported by different authors in Fe–Cr alloys hardened by NiAl intermetallics [75] and in Al–Cu alloys with non-shearable precipitates [76, 77], in which the

internal lengths associated with precipitates' interspacing is consistent with the present length-scale used in the MFDM-EVPFFT simulations for $H = 0.25$ μm. Recently, this effect was simulated and interpreted using higher order strain gradient plasticity theories [9, 12, 13].

4. Conclusions

In this study, the MFDM-EVPFFT formulation has been applied to study the reversible plasticity of two-phase laminate microstructures with plastic channels and purely elastic second phase. In contrast with CP-EVPFFT, which only describes for such microstructure a constant permanent softening associated to linear kinematic hardening depending on elastic phase volume fraction, the MFDM-EVPFFT model is able to reproduce size effects on the Bauschinger stress and a non-linear hardening associated with a more complex transient softening with inflection points during reversible plasticity. In particular, hardening mechanisms due to piling up and unpiling up of GND densities at impenetrable interfaces can be reproduced, leading to a gradual relaxation of spatial internal stress gradients during the forward and reversible strain paths.

Acknowledgements

The first author is supported by the French State (ANR) through the program "Investment in the future" (LabEx "DAMAS" grant ANR-11-LABX-0008-01) for financial support. The second author is supported by Los Alamos National Laboratory's Laboratory-Directed Research and Development (LDRD) program.

References

[1] L. Nicola, Y. Xiang, J. Vlassak, E. VanderGiessen, A. Needleman, "Plastic deformation of freestanding thin films: experiments and modeling", *J. Mech. Phys. Solids* **54** (2006), p. 2089-2110.
[2] P. J. Guruprasad, W. J. Carter, A. A. Benzerga, "A discrete dislocation analysis of the Bauschinger effect in microcrystals", *Acta Mater.* **56** (2008), p. 5477-5491.
[3] D. S. Balint, V. S. Deshpande, A. Needleman, E. Van der Giessen, "Discrete dislocation plasticity analysis of the grain size dependence of the flow strength of polycrystals", *Int. J. Plast.* **24** (2010), p. 2149-2172.
[4] C. Zhou, R. LeSar, "Dislocation dynamics simulations of the Bauschinger effect in metallic thin films", *Comput. Mater. Sci.* **54** (2012), p. 350-355.
[5] M. Jiang, B. Devincre, G. Monnet, "Effects of the grain size and shape on the flow stress: A dislocation dynamics study", *Int. J. Plast.* **113** (2019), p. 111-124.
[6] S. Waheed, R. Hao, A. Bhowmik, D. S. Balint, F. Giuliani, "A unifying scaling for the Bauschinger effect in highly confined thin films: a discrete dislocation plasticity study", *Model. Simul. Mater. Sci. Eng.* **25** (2017), no. 5, article no. 054003.
[7] M. E. Gurtin, "A gradient theory of single-crystal viscoplasticity that accounts for the geometrically necessary dislocations", *J. Mech. Phys. Solids* **50** (2002), p. 5-32.
[8] N. Ohno, D. Okumura, "Higher-order stress and grain size effects due to self-energy of geometrically dislocations", *J. Mech. Phys. Solids* **55** (2007), p. 1879-1898.
[9] N. Ohno, D. Okumura, T. Shibata, "Grain size dependent yield behavior under loading, unloading and reverse loading", *Int. J. Mod. Phys. B* **22** (2008), p. 5937-5942.
[10] N. M. Cordero, A. Gaubert, S. Forest, E. P. Busso, F. Galerneau, S. Kruch, "Size effects in generalised continuum crystal plasticity for two-phase laminates", *J. Mech. Phys. Solids* **58** (2010), p. 1963-1994.
[11] K. Danas, V. S. Deshpande, N. A. Fleck, "Compliant interfaces: a mechanism for relaxation of dislocation pile-ups in a sheared single crystal", *Int. J. Plast.* **26** (2010), p. 1792-1805.
[12] S. Wulfinghoff, S. Forest, T. Böhlke, "Strain gradient plasticity modeling of cyclic behavior of laminate structures", *J. Mech. Phys. Solids* **79** (2015), p. 1-20.
[13] S. A. El-Naaman, K. L. Nielsen, C. F. Niordson, "An investigation of back stress formulations under cyclic loading", *Mech. Mater.* **130** (2019), p. 76-87.
[14] M. Rys, H. Petryk, "Gradient crystal plasticity models with a natural length scale in the hardening law", *Int. J. Plast.* **111** (2018), p. 168-187.

[15] A. Panteghini, L. Bardella, C. F. Niordson, "A potential for higher-order phenomenological strain gradient plasticity to predict reliable response under non-proportional loading", *Proc. R. Soc. Lond. A* **475** (2019), article no. 0258.
[16] M. Jebahi, L. Cai, F. Abed-Meraim, "Strain gradient crystal plasticity model based on generalized non-quadratic defect energy and uncoupled dissipation", *Int. J. Plast.* **126** (2020), article no. 102617.
[17] I. Groma, F. F. Csikor, M. Zaiser, "Spatial correlations and higher-order gradient terms in a continuum description of dislocation dynamics", *Acta Mater.* **51** (2003), p. 1271-1281.
[18] M. Zaiser, T. Hochrainer, "Some steps towards a continuum representation of 3D dislocation systems", *Scr. Mater.* **54** (2006), p. 717-721.
[19] S. Sandfeld, T. Hochrainer, P. Gumbsch, M. Zaiser, "Numerical implementation of 3D continuum theory of dislocation dynamics and application to micro-bending", *Philos. Mag.* **90** (2010), no. 27–28, p. 3697-3728.
[20] T. Hochrainer, S. Sandfeld, M. Zaiser, P. Gumbsch, "Continuum dislocation dynamics: towards a physically theory of plasticity", *J. Mech. Phys. Solids* **63** (2014), p. 167-178.
[21] K. Schulz, D. Dickel, S. Schmitt, S. Sandfeld, D. Weygand, "Analysis of dislocation pile-ups using a dislocation-based continuum theory", *Modell. Simul. Mater. Sci. Eng.* **22** (2010), article no. 025008.
[22] A. Acharya, A. Roy, "Size effects and idealized dislocation microstructure at small scales: Predictions of a phenomenological model of mesoscopic field dislocation mechanics: Part I", *J. Mech. Phys. Solids* **54** (2006), p. 1687-1710.
[23] A. Roy, A. Acharya, "Size effects and idealized dislocation microstructure at small scales: Predictions of a phenomenological model of mesoscopic field dislocation mechanics: Part II", *J. Mech. Phys. Solids* **54** (2006), p. 1711-1743.
[24] A. Roy, S. Puri, A. Acharya, "Phenomenological mesoscopic field dislocation mechanics, lower-order gradient plasticity, and transport of mean excess dislocation density", *Modell. Simul. Mater. Sci. Eng.* **15** (2007), p. 167-180.
[25] A. Acharya, "Microcanonical entropy and mesoscale dislocation mechanics and plasticity", *J. Elasticity* **104** (2011), p. 23-44.
[26] S. Puri, A. Das, A. Acharya, "Mechanical response of multicrystalline thin films in mesoscale field dislocation mechanics", *J. Mech. Phys. Solids* **59** (2011), p. 2400-2417.
[27] S. Puri, A. Roy, "Plastic deformation of multicrystalline thin films: Grain size distribution vs. grain orientation", *Comput. Mater. Sci.* **52** (2012), p. 20-24.
[28] R. Arora, A. Acharya, "Dislocation pattern formation in finite deformation crystal plasticity", *Int. J. Solids Struct.* **184** (2020), p. 114-135.
[29] R. A. Lebensohn, A. Needleman, "Numerical implementation of non-local polycrystal plasticity using fast Fourier transforms", *J. Mech. Phys. Solids* **97** (2016), p. 333-351.
[30] A. Acharya, "A model of crystal plasticity based on the theory of continuously distributed dislocations", *J. Mech. Phys. Solids* **49** (2001), p. 761-784.
[31] A. Acharya, "Driving forces and boundary conditions in continuum dislocation mechanics", *Proc. R. Soc. Lond. A* **459** (2003), p. 1343-1363.
[32] A. Roy, A. Acharya, "Finite element approximation of field dislocation mechanics", *J. Mech. Phys. Solids* **53** (2005), p. 143-170.
[33] S. Varadhan, A. J. Baudoin, A. Acharya, C. Fressengeas, "Dislocation transport using Galerkin/least squares formulation", *Model. Simul. Mater. Sci. Eng.* **14** (2006), p. 1245-1270.
[34] V. Taupin, S. Varadhan, J. Chevy, C. Fressengeas, A. J. Beaudoin, M. Montagnat, P. Duval, "Effects of size on the dynamics of dislocations in ice single crystals", *Phys. Rev. Lett.* **99** (2007), article no. 155507.
[35] T. Richeton, G. F. Wang, C. Fressengeas, "Continuity constraints at the interfaces and their consequences on the work hardening of metal-matrix composites", *J. Mech. Phys. Solids* **59** (2011), p. 2023-2043.
[36] T. Richeton, L. T. Le, T. Chauve, M. Bernacki, S. Berbenni, M. Montagnat, "Modelling the transport of geometrically necessary dislocations on slip systems: application to single and multi-crystals of ice", *Modell. Simul. Mater. Sci. Eng.* **25** (2017), article no. 025010.
[37] S. Gupta, A. J. Beaudoin, J. Chevy, "Strain rate jump induced negative strain rate sensitivity (NSRS) in aluminium alloy 2024: Experiments and constitutive modeling", *Mater. Sci. Eng. A* **683** (2017), p. 143-152.
[38] H. Moulinec, P. Suquet, "A fast numerical method for computing the linear and non linear properties of composites", *C. R. Acad. Sci. Paris II* **318** (1994), p. 1417-1423.
[39] H. Moulinec, P. Suquet, "A numerical method for computing the overall response of nonlinear composites with complex microstructure", *Comput. Meth. Appl. Mech. Eng.* **157** (1998), p. 69-94.
[40] J. C. Michel, H. Moulinec, P. Suquet, "A computational scheme for linear and non-linear composites with arbitrary phase contrast", *Int. J. Numer. Meth. Eng.* **52** (2001), p. 139-160.
[41] R. A. Lebensohn, "N-site modeling of a 3D viscoplatic polycrystal using fast Fourier transform", *Acta Mater.* **49** (2001), p. 2723-2737.
[42] R. A. Lebensohn, R. Brenner, O. Castelnau, A. Rollett, "Orientation image-based micromechanical modelling of subgrain texture evolution in polycrystalline copper", *Acta Mater.* **56** (2008), p. 3914-3926.

[43] B. Liu, D. Raabe, F. Roters, P. Eisenlohr, R. A. Lebensohn, "Comparison of finite element and fast Fourier transform crystal plasticity solvers for texture prediction", *Model. Simul. Mater. Sci. Eng.* **18** (2009), article no. 085005.
[44] R. A. Lebensohn, A. K. Kanjarla, P. Eisenlohr, "An elasto-viscoplastic formulation based on Fast Fourier Transforms for the prediction of micromechanical fields in polycrystalline materials", *Int. J. Plast.* **32–33** (2012), p. 59-69.
[45] P. Suquet, H. Moulinec, O. Castelnau, M. Montagnat, N. Lahellec, F. Grennerat, P. Duval, R. Brenner, "Multi-scale modeling of the mechanical behavior of polycrystalline ice under transient creep", *Procedia IUTAM* **3** (2012), p. 76-90.
[46] P. Shanthraj, P. Eisenlohr, M. Diehl, F. Roters, "Numerically robust spectral methods for crystal plasticity simulations of heterogeneous materials", *Int. J. Plast.* **66** (2015), p. 31-45.
[47] S. Lucarini, J. Segurado, "On the accuracy of spectral solvers for micromechanics based fatigue modeling", *Comput. Mech.* **63** (2019), p. 365-382.
[48] A. Marano, L. Gélébart, S. Forest, "Intragranular localization induced by softening crystal plasticity analysis of slip and kink bands localization modes from high resolution FFT-simulations results", *Acta Mater.* **175** (2018), p. 262-275.
[49] S. Haouala, S. Lucarini, J. Llorca, J. Segurado, "Simulation of the Hall-Petch effect in FCC polycrystals by means of strain gradient crystal plasticity and FFT homogenization", *J. Mech. Phys. Solids* **134** (2020), article no. 103755.
[50] R. Brenner, A. J. Beaudoin, P. Suquet, A. Acharya, "Numerical implementation of static field dislocation mechanics theory for periodic media", *Philos. Mag.* **94** (2014), no. 16, p. 1764-1787.
[51] S. Berbenni, V. Taupin, K. S. Djaka, C. Fressengeas, "A numerical spectral approach for solving elasto-static field dislocation and g-disclination mechanics", *Int. J. Solids Struct.* **51** (2014), p. 4157-4175.
[52] K. S. Djaka, V. Taupin, S. Berbenni, C. Fressengeas, "A numerical spectral approach to solve the dislocation density transport equation", *Model. Simul. Mater. Sci. Eng.* **23** (2015), no. 6, article no. 065008.
[53] K. S. Djaka, A. Villani, V. Taupin, L. Capolungo, S. Berbenni, "Field dislocation mechanics for heterogeneous elastic materials: A numerical spectral approach", *Comput. Methods Appl. Mech. Eng.* **315** (2017), p. 921-942.
[54] K. S. Djaka, S. Berbenni, V. Taupin, R. A. Lebensohn, "A FFT-based numerical implementation of mesoscale field dislocation mechanics: application to two-phase laminates", *Int. J. Solids Struct.* **184** (2020), p. 136-152.
[55] S. Berbenni, V. Taupin, R. A. Lebensohn, "A fast Fourier transform-based mesoscale field dislocation mechanics study of grain size effects and reversible plasticity in polycrystals", *J. Mech. Phys. Solids* **135** (2020), article no. 103808.
[56] J. Genée, S. Berbenni, N. Gey, R. A. Lebensohn, F. Bonnet, "Particle interspacing effects on the mechanical behavior of a Fe-TiB_2 metal matrix composite using FFT-based mesoscopic field dislocation mechanics", *Adv. Model. Simul. Eng. Sci.* **7** (2020), article no. 6.
[57] N. Bertin, M. V. Upadhyay, C. Pradalier, L. Capolungo, "A FFT-based formulation for efficient mechanical fields computation in isotropic and anisotropic periodic discrete dislocation dynamics", *Model. Simul. Mater. Sci. Eng.* **23** (2015), article no. 065009.
[58] J. T. Graham, A. D. Rollett, R. LeSar, "Fast Fourier transform discrete dislocation dynamics", *Model. Simul. Mater. Sci. Eng.* **8** (2016), article no. 085005.
[59] N. Bertin, L. Capolungo, "A FFT-based formulation for discrete dislocation dynamics in heterogeneous media", *J. Comput. Phys.* **355** (2018), p. 366-384.
[60] M. F. Ashby, "Deformation of plastically non-homogeneous materials", *Philos. Mag.* **21** (1970), p. 399-424.
[61] E. Kröner, *Kontinuumstheorie der Versetzungen und Eigenspannungen*, Ergebnisse der Angewewandte Mathematik, vol. 5, Springer Verlag, Berlin, 1958.
[62] T. Mura, "Continuous distribution of moving dislocations", *Philos. Mag.* **89** (1963), p. 843-857.
[63] J. F. Nye, "Some geometrical relations in dislocated crystals", *Acta Mater.* **1** (1953), p. 153-162.
[64] E. Kröner *et al.*, "Continuum Theory of Defects", in *Physics of defects* (R. Balian, M. Kléman, J.-P. Poirier, eds.), North Holland, New York, 1981, p. 217-315.
[65] F. Willot, "Fourier-based schemes for computing the mechanical response of composites with accurate local fields", *C. R. Méc.* **343** (2015), p. 232-245.
[66] A. Acharya, "Jump condition for GND evolution as a constraint on slip transmission at grain boundaries", *Philos. Mag.* **87** (2007), p. 1349-1359.
[67] J. D. Atkinson, L. M. Brown, W. M. Stobbs, "The work-hardening of copper-silica. IV. The Bauschinger effect and plastic relaxation", *Philos. Mag.* **30** (1974), p. 1247-1280.
[68] S. F. Corbin, D. S. Wilkinson, J. D. Embury, "The Bauschinger effect in a particulate reinforced Al alloy", *Mater. Sci. Eng. A* **207** (1996), no. 1, p. 1-11.
[69] C. Rey, A. Zaoui, "Slip heterogeneities in deformed aluminium bi-crystals", *Acta Metall.* **28** (1980), p. 687-697.
[70] H. Mughrabi, "Dislocation clustering and long-range internal stresses in monotonically and cyclically deformed metal crystals", *Rev. Phys. Appl.* **23** (1988), p. 367-379.
[71] C. Rey, G. Saada, "The elastic field of periodic dislocation networks", *Philos. Mag.* **33** (1976), p. 825-841.
[72] S. Forest, "Some links between Cosserat, strain gradient crystal plasticity and the statistical theory of dislocations", *Philos. Mag.* **88** (2008), p. 30-32.
[73] K. Tanaka, T. Mura, "A dislocation model for fatigue crack initiation", *ASME J. Appl. Mech.* **48** (1981), p. 97-103.

[74] R. J. Asaro, "Elastic-plastic memory and kinematic-type hardening", *Acta Metall.* **23** (1975), p. 1255-1265.
[75] R. Taillard, A. Pineau, "Room temperature tensile properties of Fe-19wt.%Cr alloys precipitation hardened by the intermetallic compound NiAl", *Mater. Sci. Eng.* **56** (1982), p. 219-231.
[76] R. Stoltz, R. Pelloux, "The Bauschinger effect in precipitation strengthened aluminum alloys", *Metall. Trans. A* **7** (1975), p. 1295-1306.
[77] H. Proudhon, W. Poole, X. Wang, Y. Bréchet, "The role of internal stresses on the plastic deformation of the Al–Mg–Si–Cu alloy AA611", *Philos. Mag.* **88** (2008), p. 621-640.